



## Regular article

## Detection of “legbreaker” antipersonnel landmines by analysis of aerial thermographic images of the soil



Juan C. Forero-Ramírez<sup>\*</sup>, Bryan García, Hermes A. Tenorio-Tamayo, Andrés D. Restrepo-Girón, Humberto Loaiza-Correa, Sandra E. Nope-Rodríguez, Asfur Barandica-López, José T. Buitrago-Molina

School of Electric and Electronic Engineering, Engineering Faculty, Universidad del Valle, Meléndez campus, Cali Post code: 760032, Colombia

## ARTICLE INFO

## ABSTRACT

**Keywords:**  
Antipersonnel landmines  
Thermographic images  
Unmanned aerial vehicle  
Automatic classification

An automatic detection methodology for “legbreaker” Antipersonnel Landmines (APL) was developed based on digital image processing techniques and pattern recognition, applied to thermal images acquired by means of an Unmanned Aerial Vehicle (UAV) equipped with a thermal camera. The images were acquired from the inspection of a natural terrain with sparse vegetation and under uncontrolled conditions, in which prototypes of “leg-breaker” APL were buried at different depths. Remarkable results were obtained using a Multilayer Perceptron (MLP) classifier, reaching average percentages of success in detecting suspicious areas with the presence of these artifacts about 97.1 % for images acquired at 1 m from the ground and 88.8 % at higher altitudes.

## 1. Introduction

“Legbreaker” APL are explosive devices designed to harm the integrity of a person, causing muscle injuries, limb amputations or even death. Its use is very common by various terrorist groups, and it is estimated that there are more than 110 million mines spread over more than 64 countries, which affect 26,000 people each year.

Standard APL devices are expensive and difficult to obtain, which is why outlaw groups have opted to craft them. Therefore, there are many APL types varying in their composition, amount of explosive, activation mechanisms and installation depth; but the ones that tend to be more common in Colombia are the “Legbreaker” APL, being also the ones that cause the most damage to the victim because they are the most superficial. To protect the population and prevent more people from being affected by this scourge, safe, reliable, and economical solution alternatives to the problem of its detection are required with the aim of its subsequent eradication.

According to the literature consulted, the main detection techniques used correspond to Ground Penetrating Radars (GPR), Metal Detectors (MD), Multispectral Cameras and Infrared (IR) Cameras. In the first two techniques, the principle of electromagnetic coupling is used, while the

rest focus on the analysis of digital images captured in different spectral bands. In the consulted investigations that use GPR [1–6], it should be noted that these proposed methods are more suitable for the detection of mines buried more than 10 cm deep, not for surface mines such as “Legbreaker” type. In addition, the inspection with GPR must be as close as possible to the ground, increasing the level of risk for the subjects and devices involved in the detection. Research that has worked with MD [7,8] shows that this type of detection is suitable for metallic and surface mines, but poor for mines with little or no metal constitution, as expected. On the other hand, Multispectral Image Analysis is also an interesting option and is still under development for mine detection [9–12]. The successful detection results obtained by this method are above 70 %, but the not very affordable cost of multispectral cameras makes difficult its massive use still. It is also worth mentioning that there is a great variety of research that addresses the use of Unmanned Aerial Vehicles (UAV) [13–19] in which they are equipped with IR cameras, multispectral cameras or GPR, avoiding direct inspection and contact with the ground to be evaluated.

On the other hand, there are investigations in which infrared thermography [20–26] is used as a Non-Destructive Testing (NDT) method for the detection of APL; but in all of them it has been experimented

\* Corresponding author.

E-mail addresses: [juan.forero@correounalvalle.edu.co](mailto:juan.forero@correounalvalle.edu.co) (J.C. Forero-Ramírez), [bryan.garcia@correounalvalle.edu.co](mailto:bryan.garcia@correounalvalle.edu.co) (B. García), [hermes.tenorio@correounalvalle.edu.co](mailto:hermes.tenorio@correounalvalle.edu.co) (H.A. Tenorio-Tamayo), [andres.david.restrepo@correounalvalle.edu.co](mailto:andres.david.restrepo@correounalvalle.edu.co) (A.D. Restrepo-Girón), [humberto.loaiza@correounalvalle.edu.co](mailto:humberto.loaiza@correounalvalle.edu.co) (H. Loaiza-Correa), [sandra.noche@correounalvalle.edu.co](mailto:sandra.noche@correounalvalle.edu.co) (S.E. Nope-Rodríguez), [asfur.barandica@correounalvalle.edu.co](mailto:asfur.barandica@correounalvalle.edu.co) (A. Barandica-López), [jose.buitrago@correounalvalle.edu.co](mailto:jose.buitrago@correounalvalle.edu.co) (J.T. Buitrago-Molina).

under controlled laboratory conditions or with terrain prepared to achieve a certain homogeneity, making the possible results obtained by this strategy differ from a real inspection in the field. Due to the above, there is a need to develop a methodology for processing aerial thermal images, captured with a UAV, that allows the detection of “Legbreaker” APL in natural terrain with scarce vegetation, under uncontrolled conditions, all this, with the aim of constituting a much safer detection procedure, avoiding direct physical contact with the area to be evaluated and more in line with a real inspection, by taking into consideration crucial experimental variables.

## 2. Materials and methods

The developed detection system is represented by the diagram in Fig. 1, where each stage is described in next sections.

### 2.1. Construction and burial of mines

The research presented in [27] details the structure of antipersonnel mines used by armed groups in Colombia. Using this information, 8 antipersonnel mines were constructed with an external PVC cylinder 10.2 cm high and 8.7 cm in diameter (Fig. 2a). Each device was filled with 20 g of nails and 400 g of anthracite coal, a material that emulates the explosive used in these cases. Finally, a 5 mL syringe was introduced as a pump wick for each artifact (Fig. 2b). The comparison between the thermal characteristics of anthracite coal and those of TNT, a material commonly used to make these devices, is presented in Table 1. It is observed that both compounds have similar thermal characteristics, which allows anthracite coal to be used instead of the explosive as a security measure during the field tests for the acquisition of the image datasets. As TNT naturally gives off gases that are somewhat detectable in the IR spectrum, it should be noted that the change from TNT to anthracite carbon prevents these gases from being used as detection element [28]; however, this fact can ensure that the results obtained are due only to the thermal properties and morphology of the APL.

The APL built were buried at depths of 1, 5 and 10 cm, in a square soil area of 10 m side approximately with scarce vegetation, at the “Universidad del Valle” campus on January 31, 2020. Some of them were placed on the ground in order to have reference images during the acquisition experiments. The distribution details are shown in Fig. 3.

### 2.2. Image acquisition

Aerial thermographic images were acquired using a DJI Zenmuse XT camera, installed on a DJI Matrice 100 UAV. Tables 2 and 3 show the camera and UAV specifications, respectively. The experiment consisted of locating the UAV perpendicularly in each zone of the terrain (Fig. 3b), beginning at an altitude of 10 m and decreasing it by one meter each time after the image corresponding to the zone inspected was captured, and repeating this procedure until reach the height of 1 m away from the ground. In each of the inspection positions, 3 types of images were obtained in JPG, TIFF and R-JPG format. Once the nine inspection areas had been scanned, the drone was placed 1 m above the first area to take 10 images with a difference of 1 s between them. This last procedure was repeated through all the grid zones to have more images taken at 1 m from the ground, where the thermal contrast between the mines and the surrounding ground could be better captured. The final image dataset was made up of 900 aerial thermal images of the terrain under analysis, for each of the file formats, resulting from 5 inspection flights at

different predefined altitudes and at 1 m.

According to [23], a sunny day without cloudiness or rain is a suitable condition suggested for the inspection of a land with the possibility of buried antipersonnel mines; therefore, these experiments were carried out after several days of dry weather, and others, after a few days of rain in order to add variability in the soil moisture condition because this is a parameter that in excess tends to negatively affect thermographic inspection. On the other hand, according to [23] the inspection interval was between 17:00. and 18:00 since, because it is a period where the greatest thermal differences between the ground and the antipersonnel mine occur, which facilitates the detection of artifacts by thermographic inspection. Table 4 shows the environmental conditions for each inspection experiment.

### 2.3. Image preprocessing

The acquired aerial thermal images are filtered by means of a median filtering with a  $3 \times 3$  pixels kernel to reduce intrinsic noise of the camera, and, at the same time, preserving edges that helps in detecting regions likely to contain buried mines.

### 2.4. Feature extraction and selection from image dataset

For the development of the MAP detection system, 136 images with the best thermal contrast were used from a set of 198, which were acquired at a height of 1 m. From each of these images, 8 Regions of Interest (ROI) with dimensions of  $16 \times 16$  pixels were manually segmented (Fig. 4) for feature extraction: 4 ROI corresponding to regions with buried APL and the other 4 ROI to clean areas, obtaining a total of 1088 ROI. For each ROI, 22 characteristics were extracted and normalized in the range from 0 to 1: the 4 first statistical moments around the mean of intensities (mean, standard deviation, kurtosis and asymmetry), the maximum and minimum intensities, and 4 texture characteristics (energy, contrast, correlation, and homogeneity) of the co-occurrence matrices at  $0^\circ$ ,  $45^\circ$ ,  $90^\circ$  and  $135^\circ$ . After this, it was necessary to reduce the number of features and keep those with the highest discriminant power, which represents a key factor for the training stage of a learning machine. Since there are various methods that depend on the probability density function (pdf) of each feature, the *Lilliefors test* was applied to individually evaluate each feature by class, with the purpose of determining whether the extracted features have Gaussian pdf or not. Consequently, all the characteristics turned out to be Gaussian; therefore, the Fisher Discriminant Ratio (FDR) criterion and the *scalar selection* technique were used, and they determine as the most discriminant characteristics the mean of intensities, the minimum and maximum values, and the co-occurrence matrix energy at  $90^\circ$ .

### 2.5. Classifier training and operation

An MLP network, configured with 15 neurons in the hidden layer, with a sigmoidal activation function and using the *Levenberg-Marquardt* algorithm as a learning method, was selected as a classification method. For the training of this model, the set of discriminant features obtained from the 136 images with the best contrast was selected to characterize 544 ROI of “mine” class and 544 ROI of the “non-mine” class; the normalization process of those features in the range of [0,1] was carried out. The detection success percentages for each class “mine” were 99.8 % and 99.1 % for “no-mine” class, respectively, which give rise to an overall APL detection training success of 99.4 %.



Fig. 1. Diagram of the APL detection system developed.

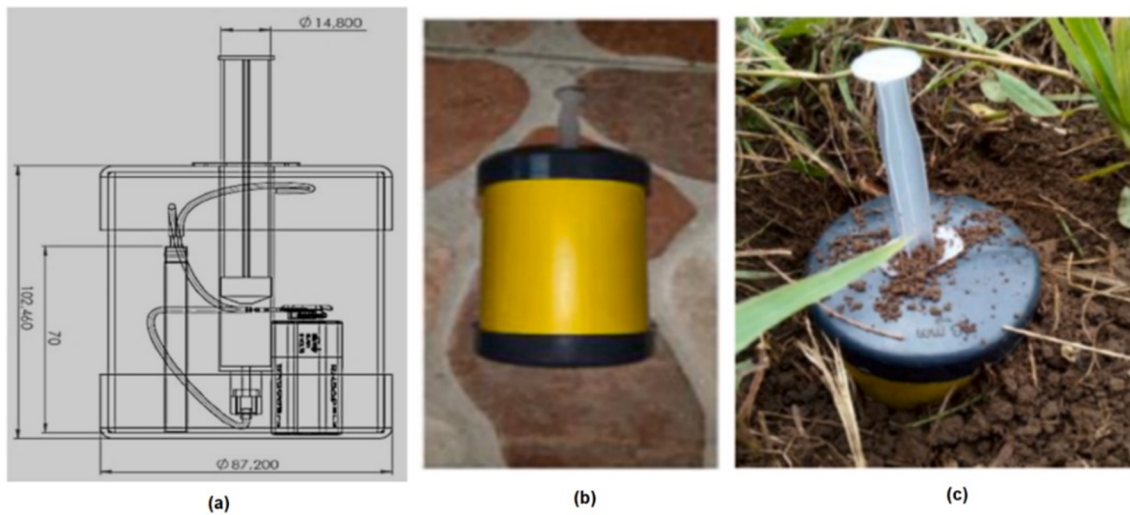


**Fig. 2.** Legbreaker APL: a) Internal and external structure of APL; b) APL built for experiment; c) APL buried.

**Table 1**

Thermal properties of TNT and anthracite coal to be used instead of the first.

Properties	TNT	Anthracite Coal
Density ( $\text{g}/\text{cm}^3$ )	1.56	1.37
Specific heat ( $\text{J}/\text{gK}$ )	1.37	1.26
Thermal conductivity ( $\text{W}/\text{mK}$ )	0.26	0.23

For the operation of the trained classifier, a sliding windowing technique was implemented in order to perform a complete scan on the image to be classified (Fig. 5a). The procedure began with the random selection of 136 images from the original set of 198 images; for each selected image, 4941 ROIs of  $16 \times 16$  pixels were extracted scanning horizontally and vertically the image every 4 pixels. Therefore, the classifier would be able to give a verdict for each ROI about the presence or not of APL in that ROI. Then, a binary image was generated from the use of neighborhoods spanning 4 ROI each: 2 vertically overlapping ROI and another 2 horizontally overlapping ROI to form a neighborhood of  $20 \times 20$  pixels. To determine to which class each of these neighborhoods belonged, the next two criteria was established: to decide if the neighborhood belongs to the “mine” class (white in the image of Fig. 5b) at least 3 ROIs must be classified as mine, otherwise the neighborhood is classified as a healthy area (black in the image of Fig. 5b); for its part, each ROI that makes up a neighborhood is categorized into the “mine” class if the classification percentage was equal to or greater than 75 %; otherwise, the neighborhood was in the “no-mine” class. In this way, the possible area with segmented APL could be obtained (Fig. 5b). Finally, the contour of this zone was superimposed on the original thermal image

(Fig. 5c) to deliver the visual result of the detection.

### 3. Results and discussion

To verify the results, the classification system was first validated with a set of 136 thermographic images acquired at an altitude of 1 m, obtaining an average success rate of 97.1 %. In this set, images acquired on different days and, therefore, in different environmental conditions were included to evaluate the performance of the classifier against uncontrolled variations, such as the soil moisture. Fig. 6 shows the MAP detection results for thermal images acquired on dry days, while Fig. 7 shows the results when the inspected soil had remaining moisture after several days of rain. For both cases, the evaluation of zones 1, 2, 3, 6, 7, 8

**Table 2**  
Specifications of the thermographic camera.

Pixels	Spectral range ( $\mu\text{m}$ )	Angular vibration range	Thermal sensitivity (mK)	Weight (g)
336x256	7.5–13.5	$\pm 0.03^\circ$	<50	270

**Table 3**  
UAV specifications.

Type	Hovering time full payload (min)	Max speed of Ascent (m/s)	Max speed of Descent (m/s)	Operating Temperature (°C)
Quadcopter	20	5	4	–10 to 40

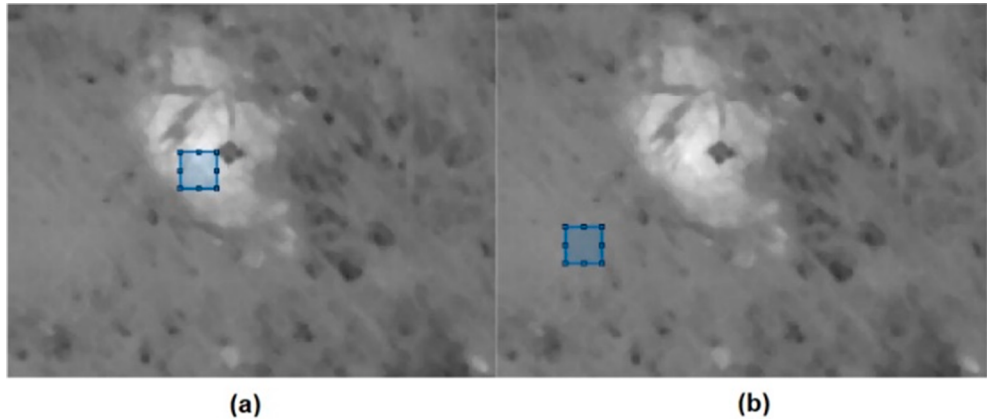
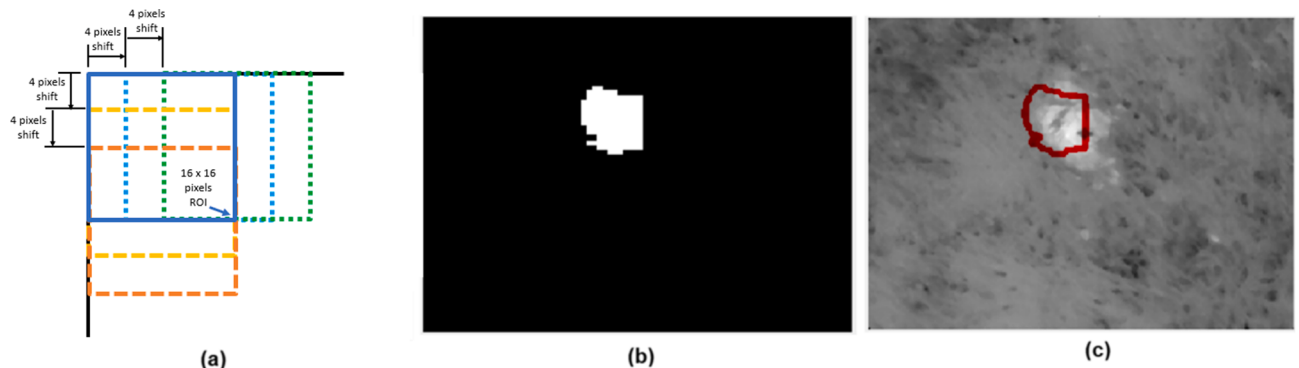
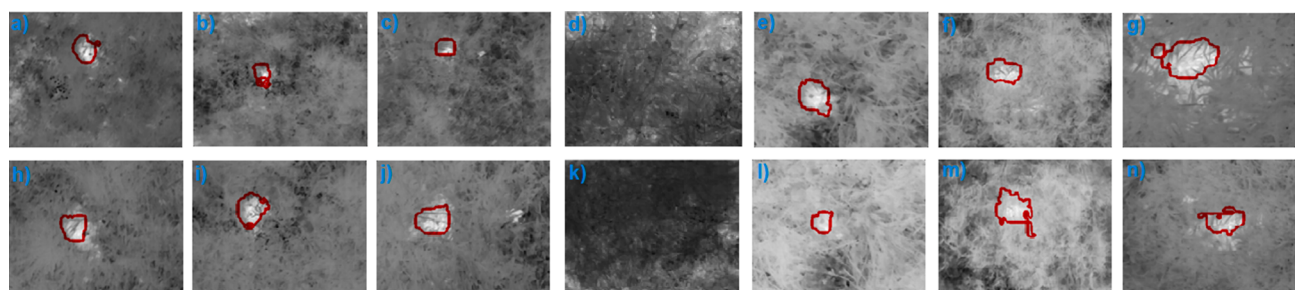


**Fig. 3.** Terrain under inspection: (a) natural terrain used; (b) APL distribution throughout the terrain.

**Table 4**

Environmental conditions for each inspection flight.

Acquisition date	Number of images	Ambient Temperature (°C)	Solar Radiation (W/m <sup>2</sup> )	Relative Humidity (%)	Wind Speed (m/s)	Ground condition
February 13, 2020	540	26.84	122.98	65.33	2.54	Dry
February 17, 2020	540	27.76	131.29	62.55	3.02	Dry
February 20, 2020	540	25.03	74.96	73.01	2	Dry
February 24, 2020	540	24.58	113.42	78.75	1.12	Wet
March 3, 2020	540	26.15	123.15	65.34	2.08	Dry

**Fig. 4.** Segmentation of ROI: (a) ROI with buried APL; (b) ROI corresponding to clean zone.**Fig. 5.** Detection example: (a) Windowing technique scheme; (b) Binary segmented image given by the classifier; (c) Detected region contour over the original thermal image.**Fig. 6.** MLP classification results for dry soil: (a) zone 1, image 1; (b) zone 2, image 1; (c) zone 3, image 1; (d) zone 6, image 1; (e) zone 7, image 1; (f) zone 8, image 1; (g) zone 9, image 1; (h) zone 1, image 2; (i) zone 2, image 2; (j) zone 3, image 2; (k) zone 6, image 2; (l) zone 7, image 2; (m) zone 8, image 2; (n) zone 9, image 2.

and 9 is presented.

Subsequently, the generalization power of the implemented MLP was preliminarily evaluated for a set of 162 images acquired at altitudes greater than 1 m, obtaining an average detection rate of 88.8 %. This is an outstanding result considering that the system was trained with

image samples acquired at an altitude of 1 m, which demonstrates the generalization power of the classifier. Figs. 8, 9, 10, 11, 12 and 13 show examples of detection for zones 1, 2, 3, 7, 8 and 9, respectively, when the acquisition altitude was varied between 1 and 10 m; Fig. 14 shows the hit rate for each acquisition altitude. These results show that, for

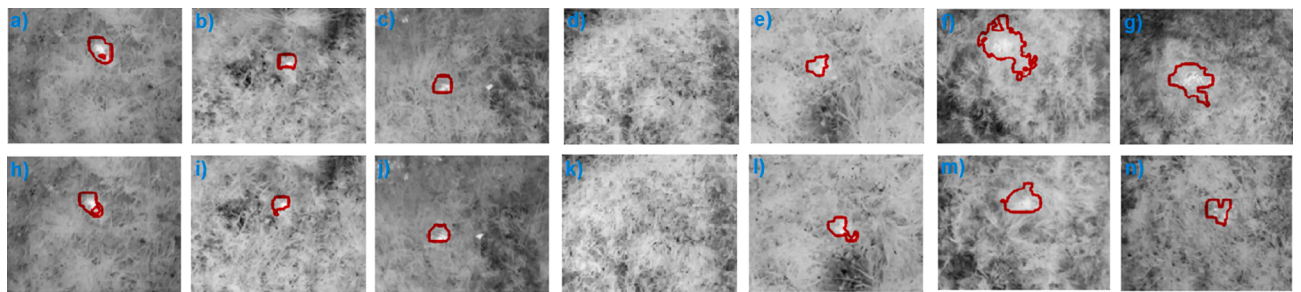


**Fig. 7.** MLP classification results for wet soil: (a) zone 1, image 1; (b) zone 2, image 1; (c) zone 3, image 1; (d) zone 6, image 1; (e) zone 7, image 1; (f) zone 8, image 1; (g) zone 9, image 1; (h) zone 1, image 2; (i) zone 2, image 2; (j) zone 3, image 2; (k) zone 6, image 2; (l) zone 7, image 2; (m) zone 8, image 2; (n) zone 9, image 2.

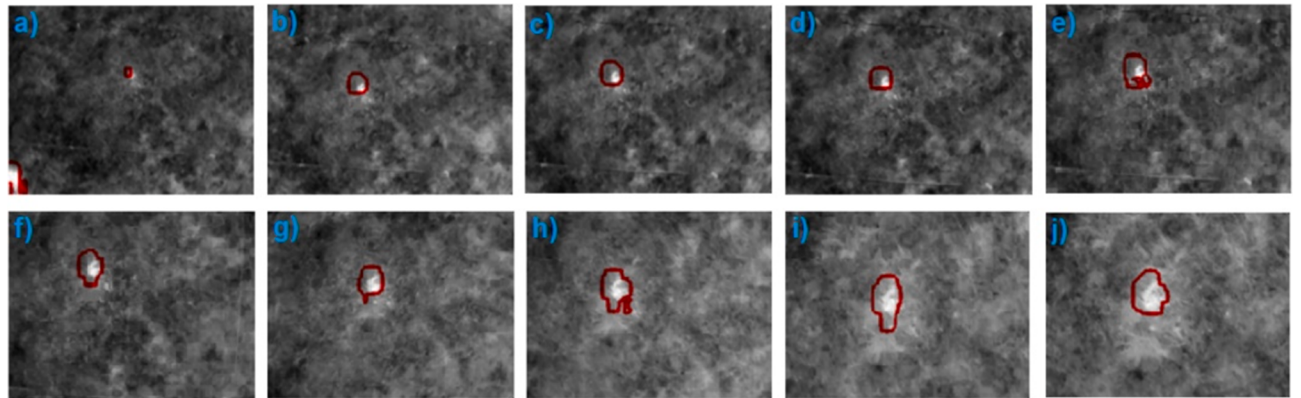


**Fig. 8.** Classification results from MLP for 10 different altitudes over zone 1 of the inspection grid: (a) 10 m; (b) 9 m; (c) 8 m; (d) 7 m; (e) 6 m; (f) 5 m; (g) 4 m; (h) 3 m; (i) 2 m; (j) 1 m.

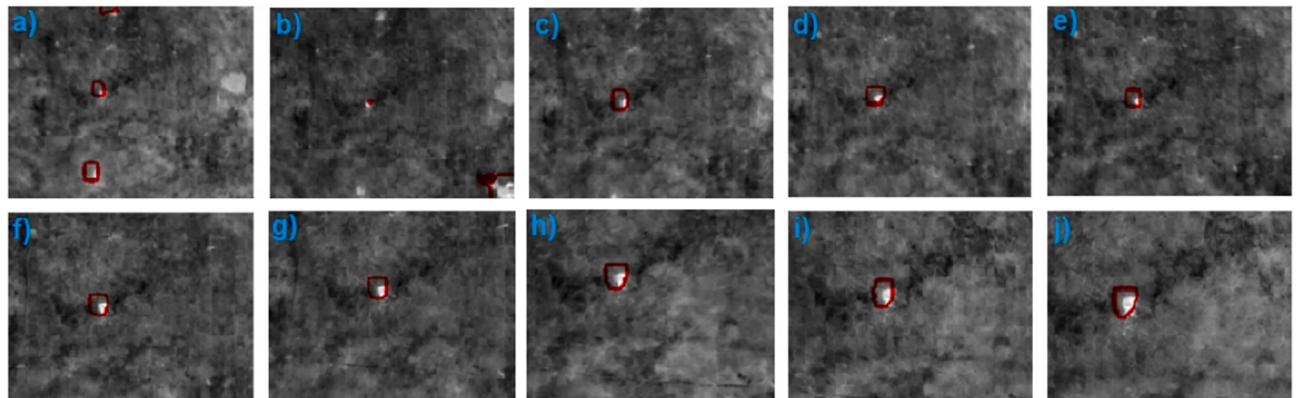


**Fig. 9.** Classification results from MLP for 10 different altitudes over zone 2 of the inspection grid: (a) 10 m; (b) 9 m; (c) 8 m; (d) 7 m; (e) 6 m; (f) 5 m; (g) 4 m; (h) 3 m; (i) 2 m; (j) 1 m.

altitudes greater than 8 m, there are some false detections, and the contour of the detected APL does not fit precisely to the real area; this trend is reversed for acquisition below 5 m where the detection of APL areas was very faithful to the actual thermal pattern in the images. However, the most important thing in this type of detection system is to ensure the lowest possible number of false negatives, even if the region segmented as suspicious does not exactly coincide with the real area of influence of the artifact.

Another important trend to highlight is the behavior of the APL that are buried at 5 and 10 cm (Zones 7, 8 and 9) compared to the superficial APL, buried at 1 cm (Zones 1, 2 and 3): the results of detection show that, for the deeper ones, there are fewer false positives and greater precision in the segmentation of the area with APL, this is largely due to the dispersion of the thermal signature, when the APL are more superficial,

the thermal pattern tends to disperse much more, due to external sources that interact with the terrain, such as vegetation, surface rocks and environmental conditions, aspects that affect deeper APL much less. In the images acquired in moisture conditions, this phenomenon is even more evident: Fig. 15 shows the success rate in APL detection for each depth from images acquired between 2 and 10 m in dry soil conditions, while Fig. 16 does for images acquired in wet soil conditions.

It should also be mentioned that the results obtained by this classification stage yielded some small, segmented areas as suspected of having buried APL; but they really corresponded to false positives. In order to present more accurate results and eliminate these false positives, a final post-processing stage was conceived that is based on digital image processing techniques for area calculation, so that an area out from a specified measurement is not considered as containing an APL.

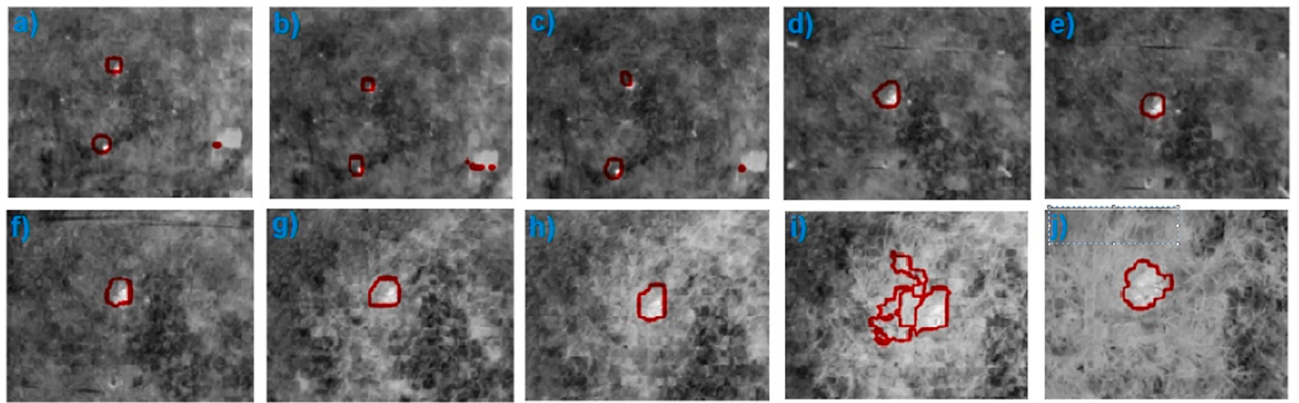


**Fig. 10.** Classification results from MLP for 10 different altitudes over zone 3 of the inspection grid: (a) 10 m; (b) 9 m; (c) 8 m; (d) 7 m; (e) 6 m; (f) 5 m; (g) 4 m; (h) 3 m; (i) 2 m; (j) 1 m.

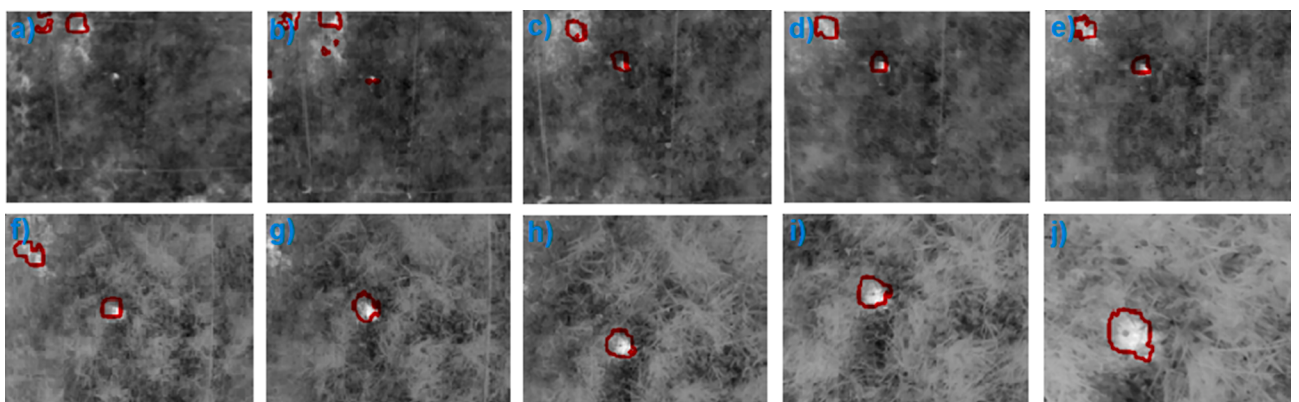


**Fig. 11.** Classification results from MLP for 10 different altitudes over zone 7 of the inspection grid: (a) 10 m; (b) 9 m; (c) 8 m; (d) 7 m; (e) 6 m; (f) 5 m; (g) 4 m; (h) 3 m; (i) 2 m; (j) 1 m.

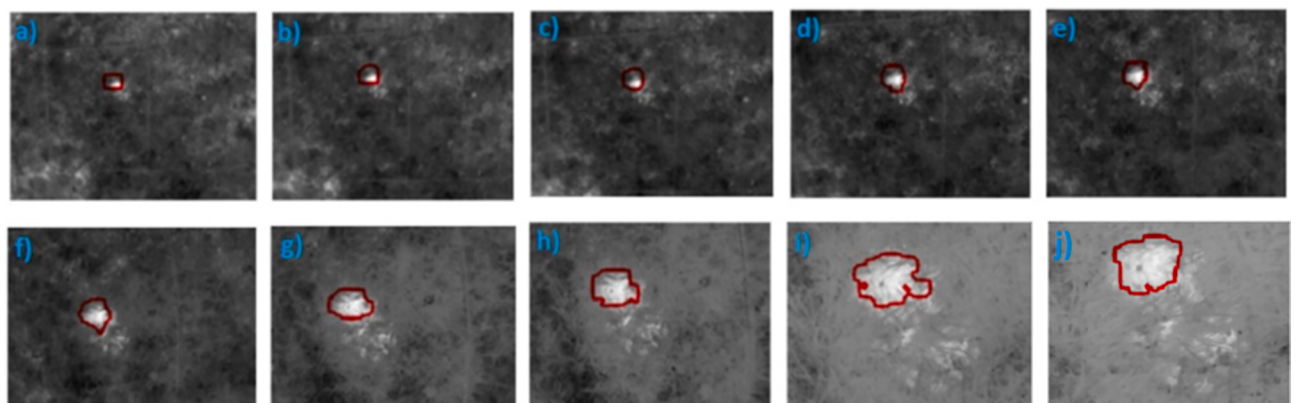


**Fig. 12.** Classification results from MLP for 10 different altitudes over zone 8 of the inspection grid: (a) 10 m; (b) 9 m; (c) 8 m; (d) 7 m; (e) 6 m; (f) 5 m; (g) 4 m; (h) 3 m; (i) 2 m; (j) 1 m.

This area value corresponds to a minimum threshold whose value is automatically calculated based on the field of view (FOV) of the camera and, therefore, on the acquisition altitude. For this, it is necessary to obtain the distance/pixel ratio ( $Lpq$ ) in the  $q$  direction (horizontal or vertical) as a function of the dimension in  $q$  of each image in pixels ( $dq$ ), the viewing angle in  $q$  of the camera ( $\theta q$ ) and the altitude from the ground ( $h$ ), according to Eq. (1).

$$Lpq = [2htan(\theta q/2)]/dq \quad (1)$$

#### 4. Conclusions

An automatic “legbreaker” APL recognition methodology was proposed based on aerial thermal images acquired at different altitudes between 1 and 10 m, and an APL classifier with a set of statistical and texture characteristics with a high discriminating power. Although the classifier of the system was trained with features extracted from the images captured at 1 m above the ground (to provide greater thermal contrast), the computational model configured was validated both with

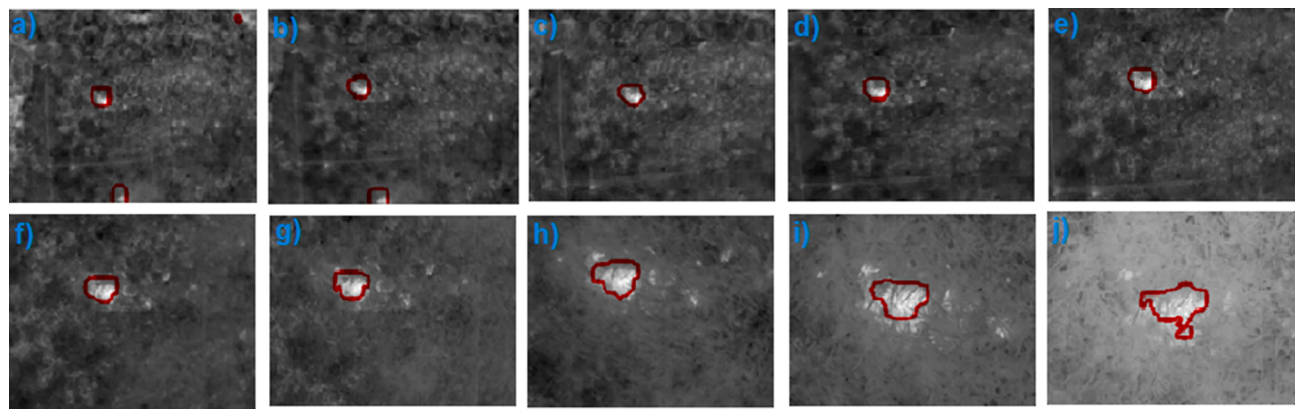


**Fig. 13.** Classification results from MLP for 10 different altitudes over zone 9 of the inspection grid: (a) 10 m; (b) 9 m; (c) 8 m; (d) 7 m; (e) 6 m; (f) 5 m; (g) 4 m; (h) 3 m; (i) 2 m; (j) 1 m.

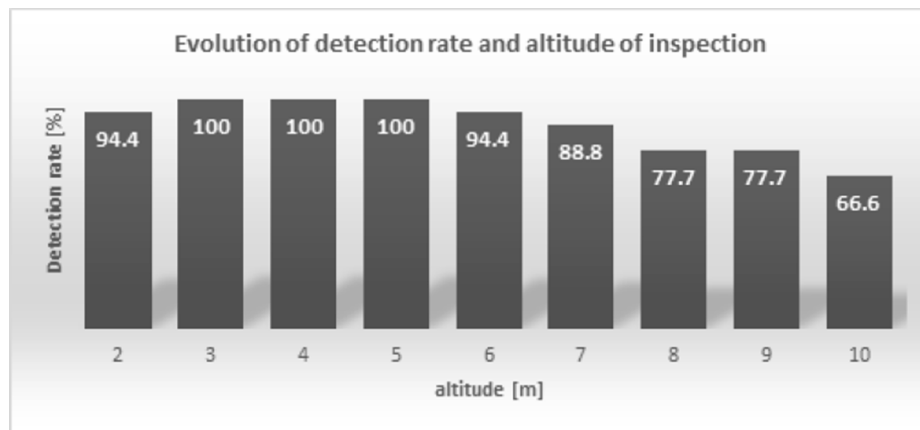


**Fig. 14.** Evolution of APL detection rates with altitude from 2 to 10 m.

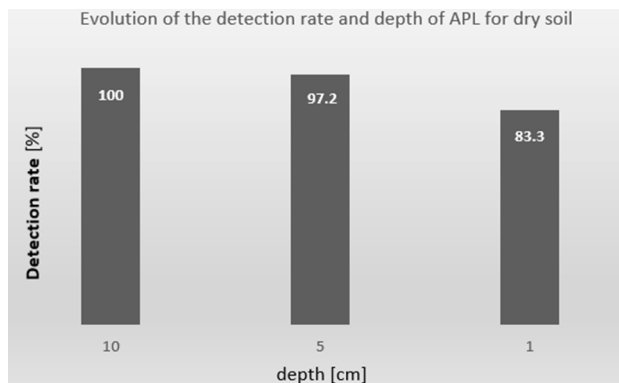


**Fig. 15.** APL detection rates for different depths for dry soil.

images taken at 1 m and at higher altitudes; the results showed an average accuracy in the detection of areas with APL of 97.1 % in the set of images at 1 m, and 88.8 % in the set of images taken at higher altitudes, demonstrating the robustness of the classification.

To achieve an experiment close to reality, the external and internal characteristics of an antipersonnel mine were established according to the bibliographic review, and 8 artisanal artifacts were built that were used to carry out the experiment. Anthracite coal was selected as the material that allows tests to be carried out in a safe environment, having thermal properties like those of the TNT explosive used by irregular armed groups to build artisanal APL. The artifacts created were buried at

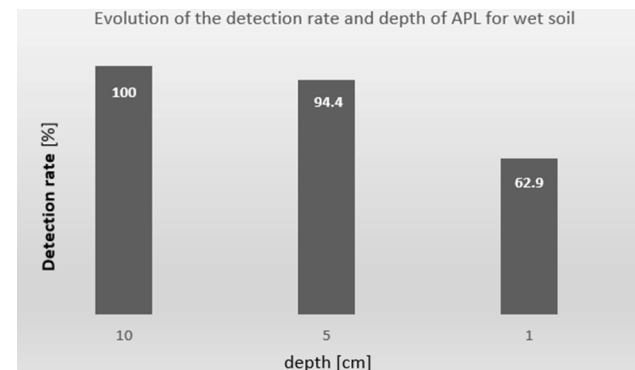


**Fig. 16.** APL detection rates for different depths for wet soil.

depths of 1, 5 and 10 cm in soil with very short vegetation, although under uncontrolled conditions of ambient temperature, humidity, solar radiation, and wind.

Excess moisture stored in the soil constitutes a condition that, although in principle hinders thermographic inspection, does not completely mask buried APL for the proposed detection system: indeed, a clear example is evidenced in the detection results of APL buried at depths of 5 cm and 1 cm, in which the average success rate in detection falls from 97.4 % to 94.4 % and from 83.3 % to 62.9 % respectively.

As future work, the short-term goal is to establish the effect on APL detection performance of including images acquired at heights greater

than 1 m in the classifier training; along with this, the use of other types of classifiers or strategies such as deep learning, and the use of multi-spectral images as base information, could improve even more the robustness of the system with respect to uncontrolled environmental conditions.

### Declaration of Competing Interest

The authors declare that they have no known competing financial interests or personal relationships that could have appeared to influence the work reported in this paper.

### Data availability

Data will be made available on request.

### References

- [1] F.H.C. Tivive, A. Bouzerdoum, C. Abeynayake, GPR Target Detection by Joint Sparse and Low-Rank Matrix Decomposition, *IEEE Trans. Geosci. Remote. Sens.* 57 (2019) 2583–2595.
- [2] J.M. Malof, D. Reichman, A. Karem, H. Frigui, K.C. Ho, J.N. Wilson, W.-H. Lee, W.J. Cummings, L.M. Collins, A Large-Scale Multi-Institutional Evaluation of Advanced Discrimination Algorithms for Buried Threat Detection in Ground Penetrating Radar, *IEEE Trans. Geosci. Remote. Sens.* 57 (2019) 6929–6945.
- [3] N. V. Nambiar, K. Gurpreet, and A. Shobha, "Automatic Landmine Detection by Pattern Trace," 2017 Int. Conf. Comput. Commun. Control Autom. ICCUEA 2017, pp. 1–5, 2018, doi: [10.1109/ICCUEA.2017.8463717](https://doi.org/10.1109/ICCUEA.2017.8463717).
- [4] fish\_0.punct]">K. Tbarki, One-Class SVM for landmine detection and discrimination, Hammamet – Tunisia (2017) 309–313.
- [5] M. W. Khalaf. Feature Extraction and Classification of Buried Landmine Signals. Boston, MA, USA, 2018, no. 2, pp. 1175–1176.
- [6] X. Shi, Z. Song, C. Wang, A Real-time Method For Landmine Detection Using Vehicle Array GPR, China Research Institute of Radio Wave Propagation Qingdao, China, 2018.
- [7] M. Zubair, M.A. Choudhry, Land mine detecting robot capable of path planning, *WSEAS Trans. Syst. Control* 6 (2011) 105–114.
- [8] Casas-Díaz, C.A.; Roa-Guerrero, E.E. Development of mobile robotics platform for identification of land mines antipersonal in different areas of Colombia. In Proceedings of the 2015 IEEE Colombian Conference on Communication and Computing, Popayan, Colombia, 13–15 May 2015; pp. 1–6.
- [9] M. Garcia-Fernandez, Y. Alvarez-Lopez, B. Gonzalez-Valdes, Y. Rodriguez-Vaqueiro, A. Arboleya-Arboleya, F. Las Heras, Recent advances in high-resolution Ground Penetrating Radar on board an Unmanned Aerial Vehicle, in: Proceedings of the 13<sup>th</sup> European Conference Antennas Propagation, Krakow, Poland, 31 March–5 April 2019.
- [10] L.-S. Yoo, J.-H. Lee, Y.-K. Lee, S.-K. Jung, Y. Choi, Application of a Drone Magnetometer System to Military Mine Detection in the Demilitarized Zone, *Sensors* 21 (2021) 3175.
- [11] I. Makki, R. Younes, C. Francis, T. Bianchi, and M. Zucchetti, "Classification algorithms for landmine detection using hyperspectral imaging," 2017 1st Int. Conf. Landmine Detect. Clear. Legis. LDCL 2017, pp. 1–6, 2017, doi: [10.1109/LDCL2017.7976930](https://doi.org/10.1109/LDCL2017.7976930).
- [12] J. S. Silva, I. Fernando, L. Guerra, J. Bioucas-dias, and T. Gasche, Landmine Detection Using Multispectral Images. 2019, vol. 19, no. 20, pp. 9341–9351.
- [13] M. Garcia, G. Alvarez, Y. Alvarez, F. Las-Heras, Analysis and Validation of a Hybrid Forward-Looking Down-Looking Ground Penetrating Radar Architecture. Area of Signal Theory and Communications, University of Oviedo, 33003 Oviedo, Spain, 2021.
- [14] J. Baur, G. Steinberg, A. Nikulin, K. Chiu, and T. S. De Smet, Applying Deep Learning to Automate UAV-Based Detection of Scatterable Landmines. 2020, NY 13902, USA, pp. 1–16, 2020.
- [15] M. Garcia, G. Alvarez, Y. Alvarez, F. Las-Heras, D. Castrillon, A. De Mitri, Portable and easily-deployable air-launched GPR scanner. 2020, University of Oviedo, 33201–33212 Gijon, Spain.
- [16] M. García-fernández, Y. Á. López, and F. Las-Heras, Airborne Multi-Channel Ground Penetrating Radar for Improvised Explosive Devices and Landmine Detection," vol. 8, 2020, doi: [10.1109/ACCESS.2020.3022624](https://doi.org/10.1109/ACCESS.2020.3022624).
- [17] R. Burr, M. Schartel, P. Schmidt, W. Mayer, T. Walter, C. Waldschmidt, Design and Implementation of a FMCW GPR for UAV-based Mine Detection. Institute of Microwave Engineering, Ulm University, 89081 Ulm, Germany, 2018.
- [18] Y. Ganesh, R. Raju, and R. Hegde, Surveillance Drone for Landmine Detection. Proc. - 2015 21st Annu. Int. Conf. Adv. Comput. Commun. ADCOM 2015, pp. 33–38, 2016, doi: [10.1109/ADCOM.2015.13](https://doi.org/10.1109/ADCOM.2015.13).
- [19] M. Garcia-fernandez, Y. Alvarez-lopez, B. Gonzalez-valdes, Y. Rodriguez-vaqueiro, A. Arboleya-arboleya, and F. Las Heras, Recent advances in high-resolution Ground Penetrating Radar on board an Unmanned Aerial Vehicle. 2019, University of Oviedo, Gijon, Spain.
- [20] S. Kaya, U.M. Lelöglü, Buried and Surface Mine Detection from Thermal Image Time Series, *IEEE J. Sel. Top. Appl. Earth Obs. Remote. Sens.* 10 (2017) 4544–4552.
- [21] Ghazali, K.H.; Jadin, M.S. Detection improvised explosive device (IED) emplacement using infrared image, in: Proceedings of the 2014 UKSim-AMSS 16th International Conference on Computer Modelling and Simulation, Cambridge, UK, 26–28 March 2014; pp. 307–310.
- [22] B. Szymanik, S. Gratkowski, Numerical and experimental validation of optimization results in microwave enhanced infrared landmines' detection, *IEEE Trans. Magn.* 51 (2015) 18–21.
- [23] B. García, A.D. Restrepo, H. Loiza, Detection of external structures of anti-personnel mines by means of thermographic inspection of soil, in: Proceedings of the 14th International Workshop on Advanced Infrared Technology and Applications (AITA) 2017, Quebec City, QC, Canada, 27–29 September 2017.
- [24] D. S, M. M, and D. G. Steeped Frequency and UWB Pulse Based Radars for Landmine Detection, pp. 2019–2022, 2019.
- [25] K. Hanton, M. Butavicius, and R. Johnson, Improving Infrared Images for Standoff Object Detection. pp. 641–646, 2009.
- [26] F. Cremer, W. De Jong, and K. Schutte, Processing of polarimetric infrared images for landmine detection. pp. 216–221, 2003.
- [27] C. Ardila, E. Gámez, P. Tirado, Los artefactos explosivos improvisados -AEI-: Una amenaza para el estado colombiano, in: J. Cubides, J. Jiménez (Eds.), Desafíos para la seguridad y defensa nacional de Colombia: Teoría y praxis, 1st ed., Bogota, Colombia, Escuela Superior de Guerra, 2017, pp. 255–309.
- [28] W. De Jong, H. Lensen, and Y. Janssen, Sophisticated test facility to detect land mines. 1999, TNO Physics and Electronics Laboratory, P0 Box 96864, 2509 JG The Hague, The Netherlands, pp. 0–9.